Monthly Notices
of the
ROYAL ASTRONOMICAL SOCIETY

Mon. Not. R. Astron. Soc. **425,** 1738–1752 (2012) doi:10.1111/j.1365-2966.2012.21654.x

The slowly evolving role of environment in a spectroscopic survey of star formation in $M_* > 5 \times 10^8\,\mathrm{M}_\odot$ galaxies since $z \sim 1$

Chad R. Greene,[1⋆] David G. Gilbank,[2⋆] Michael L. Balogh,[1] Karl Glazebrook,[3] Richard G. Bower,[4] Ivan K. Baldry,[5] George K. T. Hau,[6] I. H. Li[3] and Pat McCarthy[7]

[1] *Department of Physics and Astronomy, University of Waterloo, Waterloo, ON N2L 3G1, Canada*
[2] *South African Astronomical Observatory, PO Box 9, Observatory 7935, South Africa*
[3] *Centre for Astrophysics and Supercomputing, Swinburne University of Technology, PO Box 218, Hawthorn, VIC 3122, Australia*
[4] *Department of Physics, Institute for Computational Cosmology, University of Durham, South Road, Durham DH1 3LE*
[5] *Astrophysics Research Institute, Liverpool John Moores University, Twelve Quays House, Egerton Wharf, Birkenhead CH41 1LD*
[6] *European Southern Observatory, Alonso de Cordova 3107, Vitacura, Santiago, Chile*
[7] *Carnegie Observatories, 813 Santa Barbara Street, Pasadena, CA 91101, USA*

Accepted 2012 July 4. Received 2012 July 4; in original form 2012 April 11

ABSTRACT

We present a deep [O II] emission-line survey of faint galaxies ($22.5 < K_{\mathrm{AB}} < 24$) in the *Chandra* Deep Field South (CDFS) and the Faint Infra-Red Extragalactic Survey (FIRES) field. With these data we measure the star formation rate (SFR) in galaxies in the stellar mass range $8.85 \lesssim \log(M_*/\mathrm{M}_\odot) \lesssim 9.5$ at $0.62 < z < 0.885$, to a limit of SFR $\sim 0.1\,\mathrm{M}_\odot\,\mathrm{yr}^{-1}$. The presence of a massive cluster (MS1054−03) in the FIRES field, and of significant large-scale structure in the CDFS field, allows us to study the environmental dependence of SFRs amongst this population of low-mass galaxies. Comparing our results with more massive galaxies at this epoch, with our previous survey [Redshift One LDSS-3 Emission Line Survey (ROLES)] at the higher redshift $z \sim 1$, and with Sloan Digital Sky Survey (SDSS) Stripe 82 data, we find no significant evolution of the stellar mass function of star-forming galaxies between $z = 0$ and $z \sim 1$, and no evidence that its shape depends on environment. The correlation between specific star formation rate (sSFR) and stellar mass at $z \sim 0.75$ has a power-law slope of $\beta \sim -0.2$, with evidence for a steeper relation at the lowest masses. The normalization of this correlation lies as expected between that corresponding to $z \sim 1$ and the present day. The global SFR density is consistent with an evolution of the form $(1 + z)^2$ over $0 < z < 1$, with no evidence for a dependence on stellar mass. The sSFR of these star-forming galaxies at $z \sim 0.75$ does not depend upon the density of their local environment. Considering just high-density environments, the low-mass end of the sSFR–M_* relation in our data is steeper than that in Stripe 82 at $z = 0$, and shallower than that measured by ROLES at $z = 1$. Evolution of low-mass galaxies in dense environments appears to be more rapid than in the general field.

Key words: galaxies: dwarf – galaxies: evolution – galaxies: general.

1 INTRODUCTION

In recent years, evidence of the bimodal nature of the galaxy population has been obtained with increasing precision (e.g. Strateva et al. 2001; Baldry et al. 2004; Bell et al. 2007). Locally, the galaxy population divides quite cleanly into those which are actively star-forming and those in which star formation has been terminated, or 'quenched'. The relative mix of these two populations appears to be strongly dependent on both environment and stellar mass (M_*; e.g. Baldry et al. 2006; Peng et al. 2010). In particular, the high-mass end of the galaxy stellar mass function (GSMF) is dominated by passively evolving galaxies, while the actively star-forming population dominates at stellar masses below $M \sim 10^{10}\,\mathrm{M}_\odot$ (e.g. Pozzetti et al. 2010) at $z \lesssim 1$. Observations suggest that star formation is truncated first in the most massive galaxies (e.g. Cowie et al. 1996; Bundy et al. 2006; Pozzetti et al. 2010); however, the stellar mass function (SMF) of actively star-forming galaxies itself evolves very little (e.g. Gilbank et al. 2010a,b; Pozzetti et al. 2010).

Similarly, in the local universe the relative fraction of star-forming galaxies is strongly dependent on environment, with the densest environments dominated by passive or 'quenched' galaxies, and star-forming galaxies preferentially residing in lower density, 'field' environments. But the properties of star-forming galaxies themselves

---

⋆E-mail: cgreene@uwaterloo.ca (CRG); gilbank@saao.ac.za (DGG)

have at most a weak dependence on environment (Balogh et al. 2004; Wolf et al. 2009; Vulcani et al. 2010). Recently, several authors have claimed evidence for evolution in this environment dependence (e.g. Gerke et al. 2007; Bolzonella et al. 2010; Cucciati et al. 2010; George et al. 2011; McGee et al. 2011; Patel et al. 2011), with several observations possibly indicating *enhanced* star formation rates (SFRs) in dense regions at $z \sim 1$, under some circumstances (Elbaz et al. 2007; Cooper et al. 2008; Ideue et al. 2009; Grützbauch et al. 2011; Sobral et al. 2011). All of these effects are relatively subtle, so comparisons between works are complicated by different definitions of environment (e.g. Cooper et al. 2010; Muldrew et al. 2012), sample selection and choice of estimator [e.g. average SFR, average specific star formation rate (sSFR) = SFR/M_*, SFR of star-forming population], and star formation indicators (e.g. Gilbank et al. 2010b; Patel et al. 2011). Indeed, previous, apparently contradictory, results may be reconciled when uniform definitions are adopted (Cooper et al. 2010; Sobral et al. 2011).

Peng et al. (2010) recently presented an illuminating, phenomenological description encapsulating the environmental and stellar mass dependence of galaxy activity and suggested that these effects appear to be entirely separable. In their model, the efficiency of environment-driven transformation is independent of stellar mass and redshift, and the shape of the SMF for star-forming galaxies is universal and time independent. However, their model says nothing about the rate at which galaxies transform from the star forming to passive sequence; if this rate is slow enough, it will be observable as a population of primarily low-mass galaxies with lower than average SFR.

A direct measurement of this time-scale, which would provide important insight into the mechanisms driving this evolution, can be obtained by detecting a population of galaxies currently under the influence of 'environment quenching'. The most likely place to find such a signature is amongst low-mass galaxies (for which mass quenching is ineffective), at redshifts $z > 0.5$, when gas fractions and infall rates are high. Most spectroscopic surveys at these redshifts are limited to fairly massive galaxies (e.g. Noeske et al. 2007; Bolzonella et al. 2010; Cooper et al. 2010; Patel et al. 2011; Muzzin et al. 2012). The Redshift One LDSS-3 Emission Line Survey (ROLES) was designed to extend this work to lower stellar masses at $z \sim 1$, by searching for emission lines in K-selected samples, from fields with very deep imaging (Davies et al. 2009). This was a spectroscopic survey, conducted using the Low Dispersion Survey Spectrograph 3 (LDSS-3) instrument on the Magellan (Clay) telescope in Chile. With a custom made *KG*750 filter, redshifts and [O II] emission-line fluxes were obtained for galaxies at $0.889 < z < 1.149$ in the mass range $8.5 < \log(M_*/\mathrm{M}_\odot) < 9.5$.

ROLES demonstrated that the sSFR–mass relation evolves steadily with redshift, in a nearly mass-independent way, so the SFR density (SFRD) evolution is characterized primarily by an evolution in normalization only (Gilbank et al. 2010a). However, there is a hint that the low-mass end of the sSFR–mass relation becomes steeper at $z \sim 1$ (Gilbank et al. 2011), suggesting that the lowest mass galaxies formed their stars later, and on longer time-scales. Surprisingly, despite the small fields covered, Li et al. (2011) found a clear environmental dependence amongst the star-forming population. Star-forming galaxies in only moderately (factor of ∼15) overdense regions at $z = 1$ appear to have *higher* SFR, a result that is opposite to the (weak) trend seen locally. This is qualitatively consistent with results from some other surveys (e.g. Elbaz et al. 2007; Ideue et al. 2009; Sobral et al. 2011).

Here, we adopt the ROLES methodology (Gilbank et al. 2010a) to explore star formation and its environmental dependence amongst low-mass galaxies over the redshift range $0.62 < z < 0.885$. This provides an intermediate link between ROLES at $z = 1$ and the local Universe, using consistent galaxy selection and SFR measurement methods. Moreover, the redshift range and fields were chosen to include highly overdense regions, including the well-studied MS1054−03 galaxy cluster (e.g. van Dokkum et al. 2000; Förster Schreiber et al. 2006). Thus the data span a wider range in environment compared with the ROLES data.

This paper is presented as follows. Section 2 describes the survey and image reduction methodology, while details of the emission-line detection procedure are presented in Section 3. The basic measurements, corrections and limiting values are presented in Section 4. Our results are shown in Section 5, and we compare our results on the environmental independence of sSFR with published results at $z = 0$ and 1 in Section 6. Finally, our conclusions are summarized in Section 7. AB magnitudes are used throughout unless otherwise stated and we use a Λ cold dark matter (ΛCDM) cosmology of $H_0 = 70\,\mathrm{km\,s^{-1}\,Mpc^{-1}}$, $\Omega_\mathrm{M} = 0.3$ and $\Omega_\Lambda = 0.7$. Finally, note that all ROLES SFRs have been corrected using the empirical stellar mass-dependent relationship determined in Gilbank et al. (2010b), and described in Section 4.

2 DATA ACQUISITION AND REDUCTION

The design and implementation of the present survey are similar to our previous work at $z = 1$ (Gilbank et al. 2010a, hereafter referred to as ROLES). In this section we review the target selection criteria, observation strategy and image reduction steps.

2.1 Target selection

Targets were selected based upon their K-band magnitudes, $22.5 < K < 24$, and their photometric redshifts as provided by Förster Schreiber et al. (2006, FIRES) and Mobasher et al. (2009, CDFS). During the initial survey mask design phase, photometric redshifts were used to prioritize those targets which were expected to lie within our redshift range of $0.62 < z < 0.885$, considering the probability distribution of the photometric redshift. Galaxies with large photometric redshift uncertainties, or which were expected to lie outside our target redshift range, were also included in the mask design, with lower priority. As with ROLES, the high sampling density in these fields means that the details of the prioritization play a limited role, and the photometric redshift pre-selection does not constitute a strong prior.

Our survey consists of two pointings in the Great Observatories Origins Deep Survey (GOODS) region of the *Chandra* Deep Field South (CDFS; e.g. Wuyts et al. 2008) and one pointing in the MS1054−03 cluster region of the Faint Infra-Red Extragalactic Survey (FIRES; e.g. Förster Schreiber et al. 2006; Crawford et al. 2011) field, for a total of 18 masks. The three pointings are shown in Fig. 1 with observational targets and emission-line detections (described below) indicated.

2.2 Observations

All spectroscopic observations were obtained using the 6.5-m Magellan (Clay) telescope. Multiobject spectroscopy for our 1946 targets was provided by the LDSS-3. The spectra were dispersed by the *medium red* grism (300 lines $\mathrm{mm^{-1}}$) which has a dispersion of approximately 2.65 Å $\mathrm{pixel^{-1}}$ at 6500 Å and a relatively uniform throughput across the *KG*650 wavelength range. Combined with the plate scale of 0.189 arcsec $\mathrm{pixel^{-1}}$ and survey mask slit width

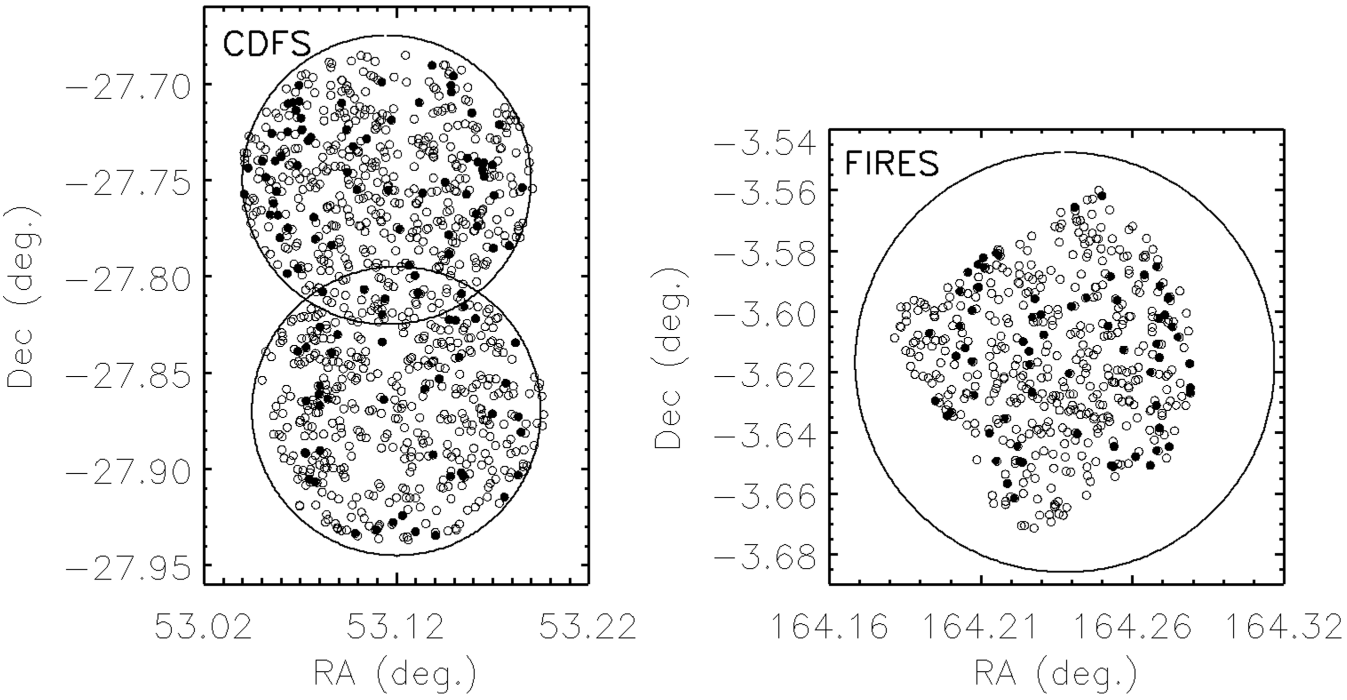

Figure 1. ROLES *KG*650 pointings in CDFS and FIRES. The ROLES pointings in CDFS are centred at (RA, Dec.) = ($03^{\mathrm{h}}32^{\mathrm{m}}27\overset{\mathrm{s}}{.}6$, $-27^{\mathrm{d}}45^{\mathrm{m}}00^{\mathrm{s}}$) and ($03^{\mathrm{h}}32^{\mathrm{m}}28\overset{\mathrm{s}}{.}8$, $-27^{\mathrm{d}}52^{\mathrm{m}}12^{\mathrm{s}}$), while the pointing in FIRES is centred at ($10^{\mathrm{h}}56^{\mathrm{m}}58\overset{\mathrm{s}}{.}26$, $-03^{\mathrm{d}}37^{\mathrm{m}}0\overset{\mathrm{s}}{.}53$). Each CDFS pointing is limited by the 8.2 arcmin diameter field of view (FOV) of the LDSS-3 spectrograph, shown as the thick black circle. The FIRES area is a 5.5 × 5.3 arcmin region which falls completely within the LDSS-3 FOV. All of the galaxies targeted are shown as open circles, while those galaxies with observed emission lines (not necessarily [O II]) are overlaid with filled circles.

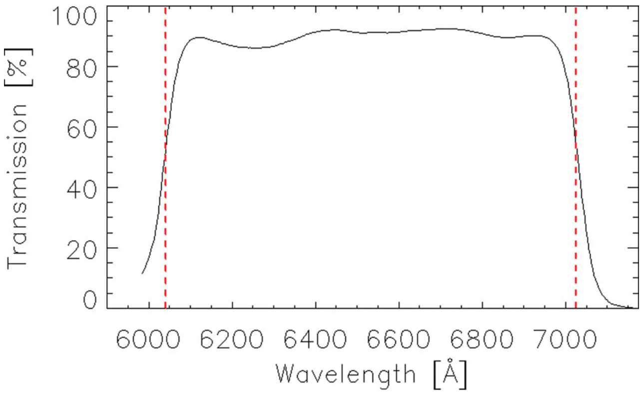

Figure 2. The transmission curve for the custom designed *KG*650 filter. The vertical dashed lines at $\lambda = 6040$, 7025 Å indicate the spectral range considered by our survey, and correspond to the full width at half-maximum (FWHM) locations of the transmission curve. Since the survey specifically targets [O II] emission at 3727 Å, the survey redshift range is also restricted by the filter FWHM and is taken to be $0.62 < z < 0.885$.

of 0.8 arcsec, the resolution is 11.2 Å full width at half-maximum (FWHM).

The spectral wavelength range was limited to approximately 650 ± 50 nm by a filter, herein referred to as *KG*650. The transmission curve for the *KG*650 filter is shown in Fig. 2. From this transmission we define our sensitivity range as $6040 \le \lambda_{\mathrm{obs}} < 7025$ Å.

The design of the survey masks was driven by the Nod & Shuffle (N&S; Glazebrook & Bland-Hawthorn 2001; Gilbank et al. 2010a) observing strategy. The principle advantage of this technique is that it allows for accurate sky subtraction at red wavelengths, where the sky brightness is dominated by rapidly varying emission lines. Target slits were 0.8 arcsec wide by 3.0 arcsec long, which allowed for nearly 200 objects to be targeted per mask given the LDSS-3 field of view (FOV) of 8.2 arcmin diameter, and the requirement that dispersed object spectra must not overlap. We used a N&S cycle time of 60 s and a slit nod distance of 1.2 arcsec.

The exposure time for each mask is shown in Table 1. From the 18 masks combined, a total of 3292 objects were targeted. This includes objects which were targeted in multiple masks, and filler objects that do not satisfy our primary selection criteria. The total number of primary targets was 2770 (including duplicates), of which 1946 are unique. These are split between 640 in FIRES and 1306 in CDFS. There were cases where slits were cut too close to mask edges, or to each other, and thus yielded unusable spectra. The number of bad slits per mask typically ranged between 2 and 7. CDFS masks 40 and 41 had an unusually large number of bad slits, with 13 and 14, respectively. For the FIRES field, three exposures per mask were acquired, while for CDFS we adopted a shorter exposure time per mask and acquired four frames per mask. The total exposure time per mask was identical for FIRES and CDFS except for CDFS masks 40 and 41 where we acquired an extra 30-min exposure for each due to time remaining in the observing programme.

2.3 Image reduction

The FITS image files created by LDSS-3 were processed through an image reduction pipeline similar to that described in the Carnegie Observatories COSMOS (Carnegie Observatories System for Multi-Object Spectroscopy) Cookbook,[1] with custom-written IDL routines to supplement the existing software when required.

---

[1] See http://obs.carnegiescience.edu/Code/cosmos/Cookbook.html

Table 1. Spectroscopic masks with their corresponding target counts, total exposure times and typical guide star seeing conditions. The two pointings in CDFS are labelled as CDFS.1 and CDFS.2. The total number of unique survey targets is 1946. The number of targets, N_{targets}, refers to the number of usable main survey spectra, excluding filler objects but including duplicates.

Mask ID	Field	N_{targets}	Exposure time (h)	Seeing (arcsec)
mask24	FIRES	115	2	0.5
mask25	FIRES	112	2	0.6
mask26	FIRES	100	2	0.63
mask27	FIRES	95	2	0.53
mask28	FIRES	99	2	0.6
mask29	FIRES	105	2	0.72
mask30	CDFS.1	191	2	1.0
mask31	CDFS.1	180	2	0.79
mask32	CDFS.1	178	2	0.8
mask33	CDFS.1	175	2	1.0
mask34	CDFS.1	178	2	1.0
mask35	CDFS.1	171	2	0.66
mask36	CDFS.2	167	2	0.86
mask37	CDFS.2	167	2	0.92
mask38	CDFS.2	164	2	0.88
mask39	CDFS.2	160	2	1.19
mask40	CDFS.2	156	2.5	0.82
mask41	CDFS.2	154	2.5	0.74

2.3.1 Initial frame combining

LDSS-3 was read out in two-amplifier mode meaning that each mask exposure consisted of two raw FITS images. These images were combined using the COSMOS 'stitch' routine with gain parameters set according to each specific amplifier and dewar parameter set to LDSS3-2. The 'stitch' routine removes bias and corrects for differences between amplifier gains in LDSS-3 so no further bias removal was necessary after this stage.

2.3.2 Bad pixel mask from charge traps & cosmic rays

A bad pixel mask (BPM) was created using N&S dark frames (N&S darks) acquired using the same N&S parameters as for the science frames. The resulting image is one which is mostly dark (predominantly read noise counts) with streaks of bright pixels indicating bad pixels created by charge being trapped by individual pixels in the CCD array. The streaks correspond to the charge shuffle distance and direction defined by the N&S strategy. A BPM was made from a N&S dark by dividing the original N&S dark frame by a 1 × 3 boxcar smoothed version (smoothing done in the direction perpendicular to the shuffle direction) of the same frame. Bad pixels appeared brighter in the ratio of the frames and were recorded as being bad in the BPM. Since several N&S darks had been acquired, they were each processed in the same manner and finally median combined into one single BPM.

As many masks were observed with only three exposures, we used the IRAF COSMICRAYS task to identify the locations of cosmic rays (CR) in each frame based upon user-defined threshold levels and CR shapes. The pixel locations were recorded as a unique BPM for each exposure, and this resulted in superior quality image stacks during median combination.

2.3.3 Wavelength calibration

The COSMOS APERTURES routine was used to make predictions of initial positions of the slit centres in each mask. These positions were compared to the actual slit centre positions as imaged through the optical path and corrected (to less than 1-pixel difference) using the ALIGN-MASK routine. The positions of known arc lines were predicted for the arc calibration frames using the ALIGN-MASK, MAP-SPECTRA and SPECTRAL-MAP routines. The COSMOS ADJUST-MAP routine was adequate for providing an initial wavelength calibration solution for most slits in a given mask. However, there remained several cases where analysis of sky emission lines revealed inaccurate calibration. For this reason an IDL routine was used to determine a third-order wavelength calibration solution to all of the slits in each mask, based on the position of these emission lines. Final emission-line position residuals were typically $\lesssim 0.7$ Å.

2.4 Creation of stacked frames

For most masks the individual exposures to be stacked were acquired on different dates. As masks were interchanged in the optical path frequently and the telescope was at different orientations while tracking the target field at different times of the year, differences in mask flexure, rotation, and shifts were introduced between one exposure and another. The transformations between science frames and an arbitrary reference frame were determined based on the common sky emission-line centroid positions in each frame. The transformations commonly required a small rotation, shifts in the X_{CCD} and Y_{CCD} directions, and on occasion a multiplicative scaling. The IRAF task GEOMAP computed these transformations, while the GEOTRAN task was used to apply them to each non-reference frame to be stacked.

The applied GEOMAP/GEOTRAN transformations accounted for differences in slit positions from one exposure frame to another. However, there were also cases where the target galaxy within a slit varied slightly in position between the frames to be stacked. To rectify this, another IDL program was written to determine and apply any further required shifts in the spectral and spatial directions based upon a list of bright emission lines identified by eye and found in each frame to be stacked. Any such shifts were typically ∼1 pixel in the X_{CCD} and/or Y_{CCD} directions.

The steps required to create the stacked signal frame from the N&S observations are described below. Individual exposure frames are labelled as A and B, and the recipe can be extended to an arbitrary number of frames.

(i) Shift frame A by 16 pixel in the spatial ('y') direction, to get a new frame A_1.

(ii) Perform the subtraction $A - A_1$ to get a new frame A_2. This is the *sky-subtracted* frame.

(iii) Shift frame A_2 by 6 pixel in the spatial ('y') direction, to get a new frame A_3.

(iv) Perform the subtraction $A_2 - A_3$ to get a new frame A_4. This frame is the 'positive' image frame.

(v) Repeat steps (i) through (iv) for all individual exposure frames.

(vi) Determine if individual frame flux scaling is necessary for each frame based upon the flux level ratios of several manually identified emission lines common between the brightest frame and the frame being scaled.

(vii) Apply further (small) frame shifting if necessary based upon the centroided positions of the identified emission lines used in step (vi).

(viii) Median add the ‘positive’ image frames, $A_4 + B_4 = C$.

The IRAF task IMCOMBINE was used to median stack the individual ‘positive’ image frames. The BPM described in Section 2.3.2, which includes identified CRs, was used to ignore pixels during the combination.

A corresponding noise frame was created in a manner similar to the stacked signal frame, as described by Gilbank et al. (2010a). In the equations below the subscripts *ij* refer to the *ij*th pixel of the frame.

(i) Apply the same frame flux scaling, determined in step (vi) of the stacked science frame creation recipe, to each *sky-added* frame.

(ii) Apply the same (small) frame shifts, determined from the locations of common bright emission lines used in step (vii) of the stacked science frame creation recipe, to each *sky-added* frame.

(iii) Stack (median add) the *sky-added* image frames to get a new frame, $|\langle \mathrm{sky}\rangle|$.

(iv) Add in the LDSS-3 read noise, R. The read noise must be added in twice since the median combined frame consists of a shifted frame added to a non-shifted frame, each containing read noise. The read noise adjusted frame is calculated as follows:

$$N_{\mathrm{indiv},ij} = \sqrt{\left(\sqrt{|\langle \mathrm{sky}\rangle|_{ij}}\right)^2 + 2(R^2)}. \tag{1}$$

(v) Scale frame $N_{\mathrm{indiv},ij}$ by the number of individual science frames used in the median combination, n_{frames},

$$N_{\mathrm{com},ij} = \frac{N_{\mathrm{indiv},ij}}{\sqrt{n_{\mathrm{frames}}}}. \tag{2}$$

(vi) Shift the frame $N_{\mathrm{com},ij}$ by 6 pixel in the spatial (‘y’) direction, to get a new frame $N'_{\mathrm{com},ij}$.

(vii) Perform the quadrature addition of these last two frames to get the final noise frame:

$$N_{ij} = \sqrt{(N_{\mathrm{com},ij})^2 + (N'_{\mathrm{com},ij})^2}. \tag{3}$$

3 EMISSION-LINE DETECTION

3.1 Creation of signal-to-noise ratio frame

To identify faint emission lines, a normalized 2D convolution kernel, k_{em}, was created which had the same Gaussian shape as a typical bright emission line (FWHM = [5.5, 3.5] pixel), and was convolved with the signal (S) and noise (N) frames to give flux-conserved, convolved signal-to-noise ratio (S/N) frames, according to

$$S_{\mathrm{conv},ij} = S_{ij} \otimes k_{\mathrm{em}} \tag{4}$$

and

$$N_{\mathrm{conv},ij} = \sqrt{N_{ij}^2 \otimes k_{\mathrm{em}}^2}. \tag{5}$$

The next step was to estimate the continuum found in the original signal frame. Similar to the convolution of the S/N frames, a convolution was again performed on the raw signal frame, using a 2D normalized averaging kernel, k_{cont}:

$$C_{ij} = S_{ij} \otimes k_{\mathrm{cont}}. \tag{6}$$

The shape of the kernel consisted of a *zero* central region (20 pixel spectral by 3 pixel spatial) and two sidebands (also each 20 pixel spectral and 3 pixel spatial). The sidebands had the same Gaussian FWHM of 3.5 pixel in the spatial direction as the emission-line kernel for their entire spectral length of 20 pixel. Convolving the kernel with the raw science frame provided an estimation of the continuum for the pixel located at the centre of the kernel. The zero region was included so that the continuum estimate was not biased by the presence of an emission line. This provides a continuum estimate that is effectively an average of the flux in the spectral and spatial directions, in the ‘wings’ of the pixel for which the continuum was being determined.

The noise due to the continuum, $N_{\mathrm{cont},ij}$, was calculated by convolving the emission-line kernel, k_{em}, with the estimation of the continuum frame, C, as follows:

$$N_{\mathrm{cont},ij} = \sqrt{C_{ij} \otimes k_{\mathrm{em}}^2} \tag{7}$$

and the total noise frame, N_{total}, was calculated by adding in quadrature the convolved raw noise frame with the convolved continuum noise estimate:

$$N_{\mathrm{total},ij} = \sqrt{N_{ij}^2 + N_{\mathrm{cont},ij}^2}. \tag{8}$$

In most cases the noise is dominated by sky line emission, but the continuum noise is not entirely negligible.

This procedure accurately accounts for statistical noise in our spectra, but may not account for low-level systematics resulting from weak charge traps, sky emission residuals (minimized but not entirely eliminated with N&S cycles of 60 s), or overlapping spectra. We analysed the *rms* fluctuations in the final science frames and compared this with the associated noise estimate, for each mask. Specifically, thirty equally spaced ‘test’ locations were chosen along the centre line (distributed in the spectral direction) of each slit in a given mask, for both the stacked science and stacked noise frames. The mean pixel value for each slit test location in the science frame was determined by taking the mean of the pixel values within two 60-pixel sidebands, located to either side of the test location. The fluctuation of the test location pixel value from the mean was found then simply by subtracting the mean value from the actual pixel value. For every slit in the mask, the science fluctuation (σ_{S}) and noise value (μ_{n}) for 30 test locations were recorded. Histograms of the science fluctuations and corresponding noise values were then fitted with Gaussians. Finally, the ratio of the best-fitting Gaussian standard deviation of the science frame fluctuations and the Gaussian mean of the noise values gave the ‘noise correction factor’ (NCF):

$$\mathrm{NCF} = \frac{\sigma_{\mathrm{S}}}{\mu_{\mathrm{n}}}. \tag{9}$$

A typical noise correction factor was ∼1.2, indicating that residual systematics amount to an additional 20 per cent on top of the statistical noise.

The final S/N frame was calculated as

$$\{\mathrm{S/N}\}_{ij} = \frac{S_{\mathrm{conv},ij} - C_{ij}}{N_{\mathrm{total},ij} \times \mathrm{NCF}}. \tag{10}$$

3.2 Emission-line finding

The central five rows of each spectrum were extracted from the 2D frame, to minimize effects near slit edges that affect line detection. For every pixel above an S/N threshold of 3, an ‘n-connected neighbour’ search was performed to locate connected neighbouring pixels that also exceed this threshold. A candidate detection then consists of two or more connected pixels; if multiple detections were separated by 5 pixel or less, they are combined into a single detection. Detections found within 3 pixel of the spectral ends of the extracted spectrum, and those that were due to overlaps of zeroth-order spectra, were excluded. The resulting list was visually inspected, and

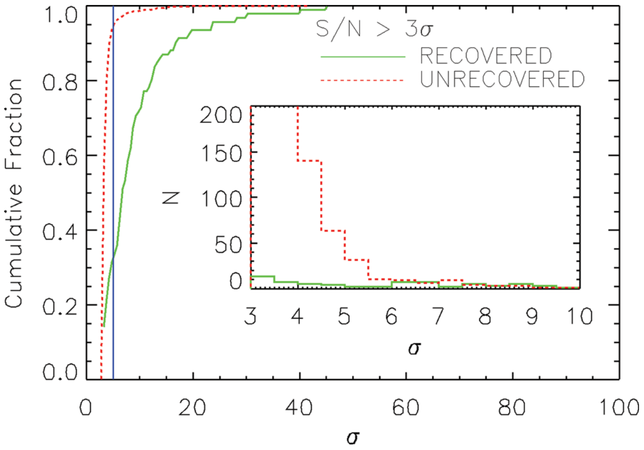

Figure 3. Main panel: the cumulative fraction of the number of recovered (solid green curve) versus spurious (dashed red curve) emission lines for galaxies which were targeted in multiple masks, as a function of significance. Inset: histogram of the number of recovered and spurious emission lines. This demonstrates that 95 per cent of spurious detections occur below 5σ (highlighted as the solid vertical blue line).

obvious false detections (due in general to overlapping spectra or missed CRs) were manually removed.

3.2.1 *Catalogue purity*

The 3σ (S/N $\geq$ 3) catalogue was internally tested in two ways to determine the purity, following Gilbank et al. (2010a). We first consider the reproducibility of emission lines for the 412 galaxies that were targeted on more than one mask. For these galaxies, detection lists were compared and emission lines were considered to match if their wavelengths were within $\pm$6.5 Å (2.5 pixel) of each other. If a detection was found in all of the masks the galaxy was targeted in, then it was considered fully recovered; otherwise it was considered spurious. This is therefore a conservative estimate of the purity. The results of this test are shown in Fig. 3 where it is clear that 95 per cent of spurious detections occurred in detections below 5σ.

An independent test of purity is to consider spectra for which more than one candidate is detected. The wavelengths of these candidates were compared with expected sets of lines, which are likely to appear in only a small number of combinations: the H$_\beta$-[O III] complex (H$_\beta$, [O III]$_{4959}$, [O III]$_{5007}$) and the [Ne III]$_{3869}$, [O II]$_{3727}$ pair. Candidates were considered real detections if their line ratios matched one of these combinations. In the case that the lines did not correspond to an expected set, the line with the highest significance was considered real, while the next highest significance line was considered spurious; lower significance lines were omitted for the purpose of this test. Fig. 4 shows the S/N distribution of these real and spurious lines; ~97 per cent of spurious lines have significance less than 5σ.

From these tests, we conclude that >95 per cent of false detections occur below a significance threshold of S/N $\geq 5\sigma$; thus we only consider detections above this limit in our analysis.

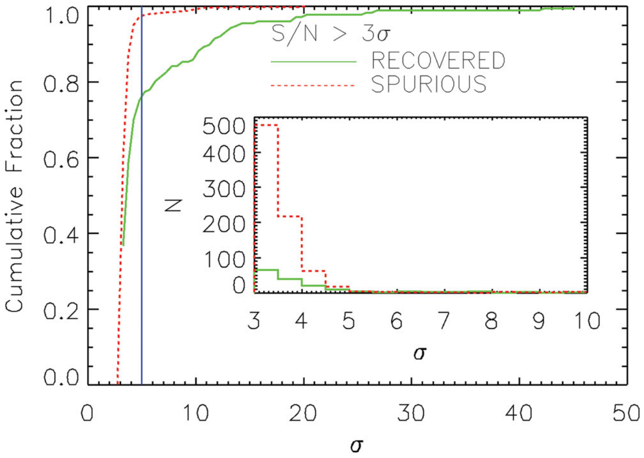

Figure 4. Main panel: the cumulative fraction of the number of recovered (solid green curve) versus spurious (dashed red curve) emission lines for galaxies which contain at least two emission lines and lead to self-consistent redshifts, as a function of significance. Inset: histogram of the number of recovered and spurious emission lines providing self-consistent redshifts for the galaxies containing them. It is clear from the cumulative fractions that ~97 per cent of spurious detections occur below 5σ (highlighted as the solid vertical blue line).

3.3 Emission-line flux determination

Flux calibration was based on the spectrophotometric standard star HD 49798 (Bohlin & Lindler 1992). Emission-line fluxes and their errors were measured from the stacked raw science frames with the continuum estimation removed, and the stacked raw noise frames. The BPMs were incorporated to eliminate bad pixels and CRs. For each detection, the centroid position of the flux was found within a 15 × 17 pixel box, initially centred on the location of the highest significance pixel in the emission line. The total emission-line flux was taken to be the sum of flux within a 7 × 5 pixel region about this centroid. The line flux error was calculated for the same pixels, based on the noise spectrum.

To account for varying photometric conditions, we compare the flux in the continuum measured from the spectra on each mask with photometric data from public catalogues. For the CDFS field we use the *R*-band magnitudes from FIREWORKS (Wuyts et al. 2008), which covers almost exactly the same wavelength range as our spectroscopy. For the FIRES field, the available photometry does not include *R* magnitudes, so we interpolated between the *Hubble Space Telescope* (*HST*) Wide Field Planetary Camera 2 (WFPC2) *F*606*W* and *F*814*W* filters. For each mask we calculate the average offset between the flux in our spectra and the continuum flux measured from the imaging. We use this to identify the most photometric mask in each field, and the offsets from this mask for all of the others. We then correct the flux calibration for the non-photometric masks, to match this reference frame. The correction is typically ~0.5 mag, with a maximum of 1 mag.

We take advantage of galaxies within our 5σ line list that were imaged on multiple masks, to further check the consistency of the flux calibration and our uncertainty estimates. The flux differences for separate observations were determined and plotted as a function of line flux, as shown in Fig. 5. As expected, the matching line flux differences are scattered about zero. The significance of each difference is obtained by dividing by the flux uncertainties added in quadrature. The significance distribution has a standard deviation of $\sigma \sim 1.28$, but a Kolmogorov–Smirnov test cannot distinguish between this distribution and a normal distribution with $\sigma = 1$. Thus we conclude that uncertainties in relative flux calibration from mask to mask are negligible.

We looked for a correlation between the flux difference compared with the photometry and galaxy size. While there does appear to be

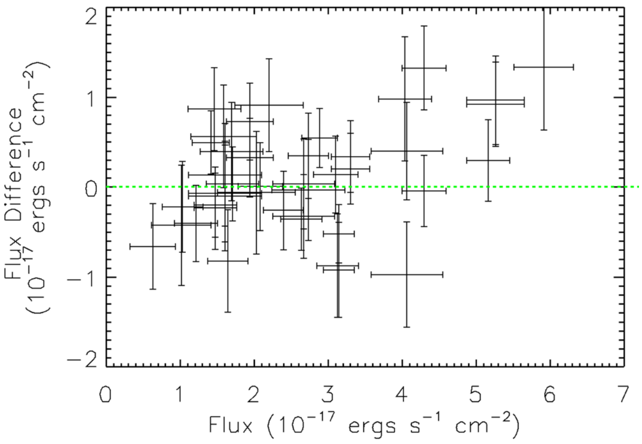

Figure 5. The difference in $\geq 5\sigma$ emission-line fluxes for matching detections found in multiply imaged galaxies as a function of line flux. The zero difference line is shown as the horizontal green dashed line.

a correlation in the expected sense, that larger galaxies are missing more flux in our spectroscopy, there is a lot of scatter from object to object. We have elected therefore not to apply an aperture correction, but note that the fluxes for our largest galaxies are likely underestimated. Only three of our spectra overlap with spectra obtained by Vanzella et al. (2008); while this comparison shows that our flux calibration is consistent with theirs, there are not enough objects in common to state this with a high degree of confidence. Thus we expect that our line fluxes are dominated by this systematic uncertainty in flux calibration, which is likely at least a factor of ∼2 with a dependence on galaxy size.

The wavelength-dependent flux limit was determined for each survey mask from the associated noise propagated through the analysis pipeline. For each mask, the average noise spectrum σ_λ was determined from all the dispersed spectra in the mask, and secure detections were then defined as those brighter than $5\sigma_\lambda$. Fig. 6 shows the flux of all detected lines, and the average $5\sigma_\lambda$ noise level for all masks. Unless otherwise stated, analysis in this paper excludes lines that fall below the average flux limit shown here, to enforce a uniform limit.

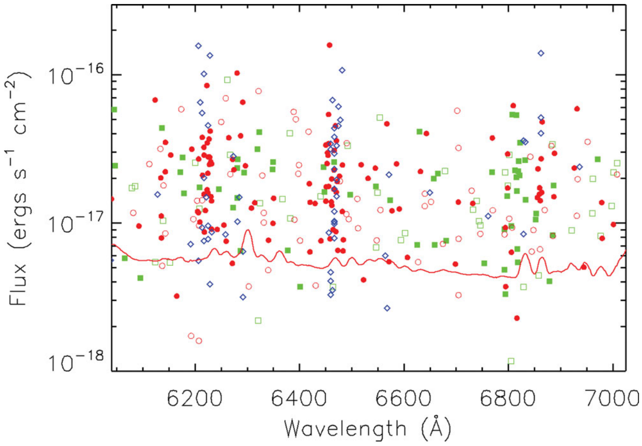

Figure 6. Fluxes for emission lines detected with 5σ significance are shown as a function of wavelength. Detections are divided into the CDFS ROLES (solid/open red circles), FORS2 (blue diamonds) and FIRES (solid/open green squares) fields. The average $5N_{ij}$ noise flux limit of all masks is overplotted as a solid line.

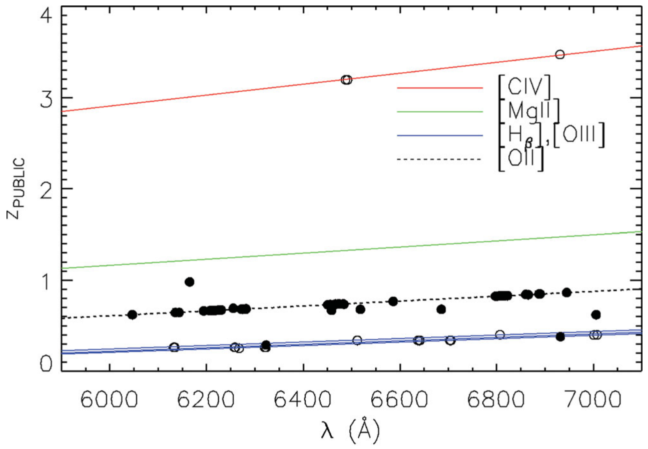

Figure 7. The published redshift, where available, is shown for galaxies with candidate emission lines in our catalogue as a function of the line wavelength. Angled lines show the relation expected for seven different emission lines as indicated; in particular the black dashed line indicates our target line of [O II]. Filled circles correspond to detections with $\mathcal{L}$[O II] > 0.9.

3.4 Line identification

For galaxies in the $\geq 5\sigma$ catalogue where more than one emission line was detected with an appropriate wavelength separation, identification was straightforward. However, there are only 41 such candidates, 15 of which are identified as [O II]. The remainder of the catalogue consists of single emission lines, for which we rely on the photometric redshift probability distribution functions (PDFs) to identify the line, as described in Gilbank et al. (2010a). The relative likelihood of a line being [O II] was assigned to each detection in our 5σ catalogue by determining the ratio of the probability of the emission line being [O II] to the total probability of being either [Mg II], [C IV] or one of the Hβ-[O III] complex. The probabilities were calculated by integrating the photometric redshift PDFs over the redshift ranges corresponding to the lines of interest in our spectral window.

For a few lines, publicly available spectroscopy covering a larger wavelength range are available; nine from Crawford et al. (2011, MS1054−03) and 73 from Wuyts et al. (2008, FIREWORKS) have secure redshifts. Fig. 7 shows these secure redshifts as a function of the wavelength of the detected emission line in our sample. Straight lines indicate the redshift–wavelength relation for different emission lines, including [O II] (black dashed line). The detections denoted by solid symbols were those which had an integrated photometric redshift probability of being [O II]. Most of the emission lines which had a high probability of being [O II] ($\mathcal{L}$[O II] > 0.9) are confirmed as such from the public redshift. Of the 82 matched detections shown in the figure only three appear inconsistent with their published redshift, suggesting that the purity of our sample is over 95 per cent.

3.5 Final 5σ catalogue

The final catalogue contains all detections with S/N $\geq$ 5, and a redshift determined following the line identification procedure described above. The detections were also given a *line quality* flag as follows.

(0) Line is not likely [O II] based on the photometric redshift PDF, and there is no existing public redshift.

(1) Photometric redshift is consistent with the detection being [O II].

(2) Photometric redshift is consistent with the detection being [O II], confirmed by detection of [Ne III].

(3) Photometric redshift is consistent with the detection being [O II], confirmed by a published redshift.

4 ANALYSIS

Spectroscopic redshifts determined for the galaxies in our 5σ line list, as well as photometry in the CDFS field from the FIREWORKS catalogue (Wuyts et al. 2008; U_{38}, B_{435}, B, V, V_{606}, R, i_{775}, I, z_{850}, J, H, K_s, [3.6], [4.5] and [8.0]), and in the FIRES field (Förster Schreiber et al. 2006; U, B, V, V_{606}, I_{814}, J_s, H and K_s), served as inputs to the stellar PEGASE.2 (Fioc & Rocca-Volmerange 1997) population models, as described in Glazebrook et al. (2004). The models were fitted to aperture magnitudes, and the final stellar masses[2] were subsequently scaled according to the total K_s magnitude.

Emission-line luminosities were first converted to 'fiducial' SFRs (SFR$_f$), starting from the Kennicutt (1998) relation:

$$\mathrm{SFR_f}\ (\mathrm{M_\odot\ yr^{-1}}) = \left[\frac{10^{0.4A_{\mathrm{H}\alpha}}}{0.5}\right]\left[\frac{7.9\times10^{-42}}{1.82}\right]\left[L_{[\mathrm{O\,II}]}(\mathrm{erg\ s^{-1}})\right], \tag{11}$$

where the factor of 1.82 accounted for the conversion from a Salpeter initial mass function (IMF; Salpeter 1955) to the BG03 IMF (Baldry & Glazebrook 2003), and we assume $A_{\mathrm{H}\alpha} = 1$. In practice, $A_{\mathrm{H}\alpha}$ and the other coefficients in equation (11) are likely to depend strongly on the galaxy stellar mass. We therefore use the empirical correction advocated by Gilbank et al. (2010b, equation 8), based on analysis of the Sloan Digital Sky Survey (SDSS):

$$\mathrm{SFR}\ (\mathrm{M_\odot\ yr^{-1}}) = \frac{\mathrm{SFR_f}}{\{(a)\times\tanh\left[(X+b)/c\right]+d\}}, \tag{12}$$

where $X = \log(M_*/\mathrm{M_\odot})$, $a = -1.424$, $b = -9.827$, $c = 0.572$ and $d = 1.700$. We apply this correction to all SFRs reported in this paper.

This SFR estimate assumes that the [O II] emission arises from gas ionized by massive stars; any contribution from an active galactic nucleus (AGN) would reduce the SFR. We would not expect AGN to contribute significantly in such low-mass galaxies; in Gilbank et al. (2010a) we confirmed from analysis of mid-infrared colours and *Chandra* point sources that AGN were entirely negligible in that $z = 1$ sample. We will therefore also neglect AGN contamination, except when we include higher mass galaxies from other surveys (Section 4.1).

4.1 Extension of the survey to higher masses

We supplement our survey with brighter (more massive) galaxies, primarily from publicly available Very Large Telescope (VLT)/FORS2 spectroscopy overlapping our CDFS sample area, from (Vanzella et al. 2008). Their sample was a colour and photometric redshift selected catalogue with targets found between the redshift ranges of $0.5 \lesssim z \lesssim 2$ and $3.5 \lesssim z \lesssim 6.3$. We selected only those targets which were found within the LDSS-3 FOV centred on our CDFS field pointings, and which fell within our redshift range of $0.62 < z < 0.885$. Their observation masks used 1-arcsec slits (compared to 0.8 arcsec for ROLES) and exposure times for each mask were typically $\geq$4 h. Hereafter this higher mass sample is referred to as FORS2.

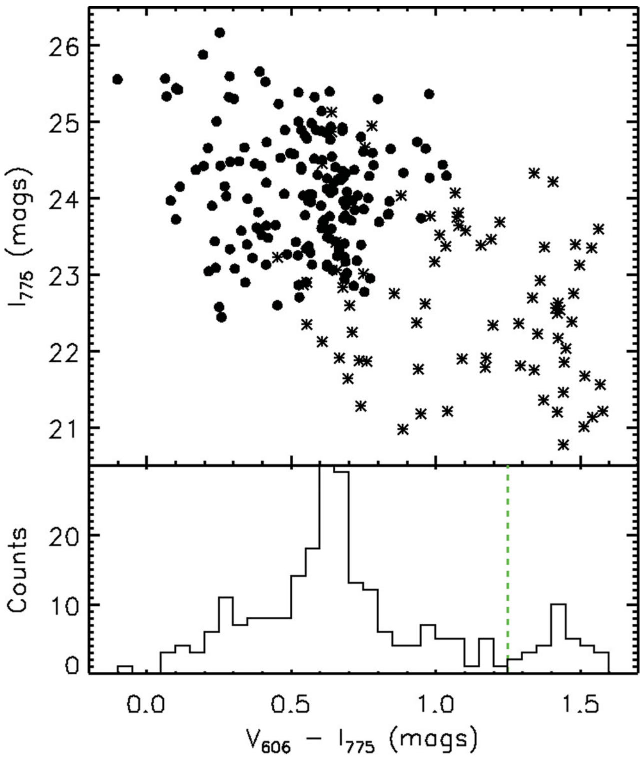

Figure 8. The colour–magnitude diagram of the CDFS and FORS2 targets is shown. Upper panel: our targets in the CDFS are shown as solid black circles, while the public FORS2 data are represented by black asterisks. Bottom panel: the overall distribution of $V_{606} - I_{775}$ colour is shown. The red-sequence cut is shown as the vertical green dashed line; we exclude galaxies redder than this limit from the remainder of our analysis.

For these massive galaxies, there is more concern that the emission lines could arise from AGN or LINER emission, rather than star formation. As in ROLES, we therefore exclude red-sequence galaxies from the sample, using a colour–magnitude diagram (CMD) consisting of bands which bracket the 4000 Å break at $z \sim 0.75$. Fig. 8 shows the characteristic bimodal colour distribution of galaxies in our CDFS and FORS2 samples; while all our low-mass targets are in the blue cloud, a subset of the FORS2 galaxies are on the red sequence, with $V_{606} - I_{775} > 1.25$ mag.

For each FORS2 emission line we calculated $V_{\max}$ as before (with a typical value of 4.7×10^4 Mpc^3). The K-magnitude binned FORS2 completeness was determined in the same way as for our data, and the results are shown in Fig. 10. We extracted spectroscopic redshifts, line identifications and quality flags, and 1D spectra for these galaxies. [O II] emission-line fluxes were measured from the 1D spectra in the same way as for our own data. A constant 4σ noise flux limit of 6×10^{-18} erg s^{-1} cm^{-2} was adopted, approximately the same as the average noise flux limit for the rest of our sample (see Fig. 6).

4.2 Completeness

As for ROLES, we characterize our spectroscopic completeness as follows. For each field, all photometric redshift PDFs corresponding to galaxies within our target fields were first binned by K magnitude. Within each bin the PDFs were summed, giving the total redshift

---

[2] PEGASE.2 only accounts for luminous stars in its determination of stellar mass. Thus stellar remnants such as white dwarfs, neutron stars and black holes were not included.

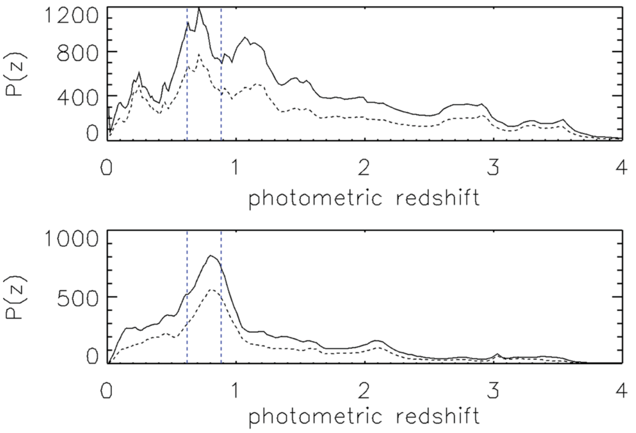

Figure 9. Upper panel: summation of all photometric redshift PDFs within the LDSS-3 FOV and with $22.5 < K < 24$ (black curve) compared with the summation of those photometric redshift PDFs corresponding to galaxies targeted in this survey (lower green curve), for the CDFS field. Lower panel: same as the upper panel, corresponding to the FIRES field.

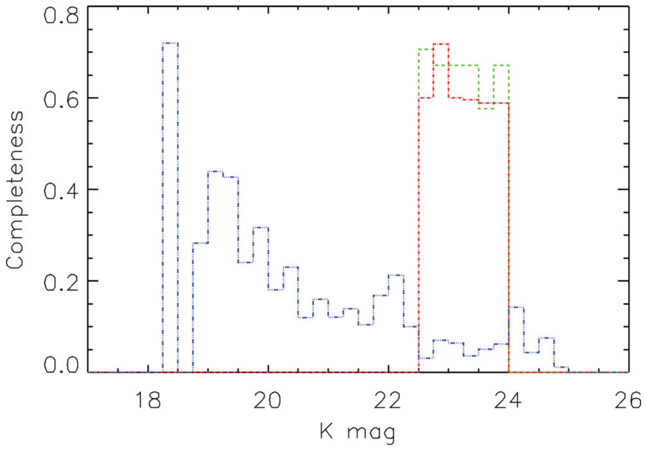

Figure 10. Completeness histograms for our surveys in the CDFS and FIRES are shown as the red and green lines. We also include existing FORS2 data for brighter galaxies, shown as the blue histogram.

distribution for all galaxies in each bin, $P_K(z)$. The summed redshift distribution in each bin was then integrated over the redshift of interest here, $0.62 < z < 0.885$. The process was then repeated for only those galaxies that were successfully targeted (i.e. the slit was successfully extracted), and the ratio of this to the total distribution yields the targeting completeness. The redshift PDFs of targeted and candidate galaxies are shown in Fig. 9.

The resulting completeness is high, ∼70 per cent, and independent of K magnitude. This is shown in Fig. 10 with the CDFS field represented by the red dashed line and the FIRES field denoted by the green dashed line. The figure also includes spectra for brighter galaxies from the public domain, discussed in Section 4.1.

4.3 Redshift distribution and definition of dense environments

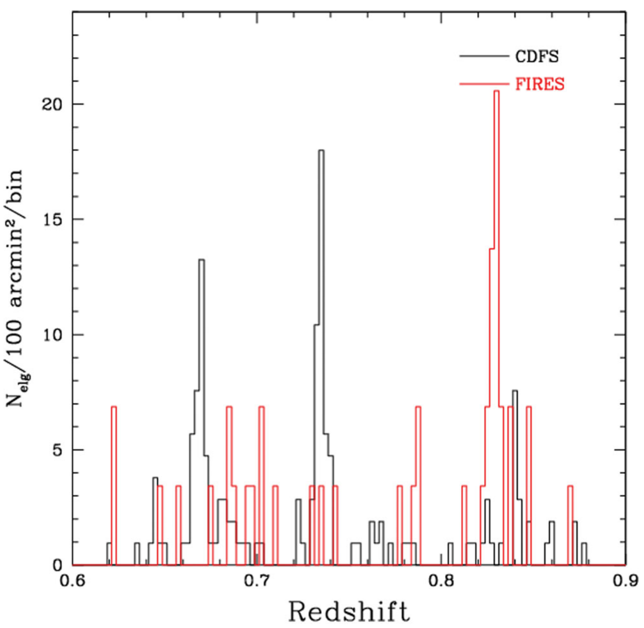

Figure 11. The redshift distribution of emission-line galaxies in our sample. The distributions are normalized to an area of 100 arcmin^2, close to the area of the CDFS and ∼3.6 times larger than the FIRES field. Large-scale structure, due to the known walls in the CDFS and the cluster MS1054−03 in the FIRES field, is identifiable as three narrow redshift peaks.

The redshift distribution of our emission-line galaxies is shown in Fig. 11. Two prominent peaks in this distribution at $z \sim 0.68$ and $z \sim 0.73$ correspond to the well-known 'wall-like' structures in the CDFS (Gilli et al. 2003; Le Fèvre et al. 2004; Vanzella et al. 2005; Ravikumar et al. 2007). We associate all CDFS galaxies with $|z - 0.668| < 0.016$ and $|z - 0.735| < 0.009$ with these structures. As traced by our low-mass galaxy sample, this structure is spread fairly uniformly over the LDSS-3 FOV, without an apparent density gradient or central concentration. The rest-frame velocity dispersion of emission-line galaxies in each of these structures is 970 and 430 km s^{-1}, respectively. The other important structure, at $z \sim 0.83$, is the MS1054−03 cluster, in the FIRES field (Förster Schreiber et al. 2006); all galaxies in the field and within $\Delta z = 0.02$ of this redshift are associated with the cluster. The rest-frame velocity dispersion of these emission-line galaxies is 1300 km s^{-1}, in good agreement with van Dokkum et al. (2000). Together, these three subsets of galaxies are referred to as 'dense environments' for the subsequent analysis. Combined, the subsample comprises 112 galaxies, 23 of which are associated with the MS1054−03 cluster. The remaining galaxies are referred to as the 'field'; it now represents an underdense sample relative to the average of our full sample. We will show in Section 5.2 that both the CDFS 'walls' and the MS1054 cluster are comparably overdense, by a factor of at least 7 relative to the field, and probably more like a factor of $\gtrsim$45.

4.4 [O II] luminosity, stellar mass and SFR limits

The stellar mass limit of our sample is determined from the scatter in the correlation between K magnitude and stellar mass shown in Fig. 12. The horizontal line shows our limiting selection magnitude of $K = 24$. Based on the scatter in this relation, the sample is nearly (>90 per cent) complete in stellar mass for $\log(M_*/\mathrm{M}_\odot) \gtrsim 8.85$. We take this to be our 2σ mass completeness limit; the sample extends to lower masses, but is systematically missing galaxies with high M/L_K ratios.

The average 5σ [O II] flux limit as a function of wavelength was shown in Fig. 6. The sample is statistically complete for fluxes as low as $\sim 5 \times 10^{-18}$ erg s^{-1} cm^{-2}. Considering our low-redshift bound of $z \sim 0.62$, the corresponding [O II] luminosity limit at

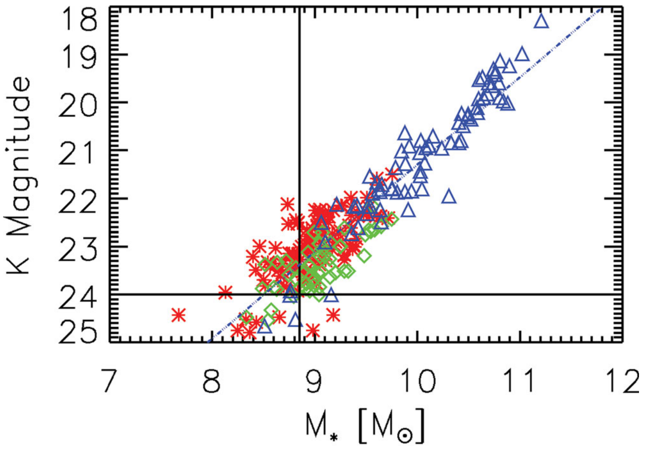

Figure 12. K magnitude as a function of stellar mass for emission-line galaxies in our two survey fields (red for CDFS and green for FIRES), supplemented with the more massive FORS2 galaxies (blue triangles). The solid lines show the K magnitude and adopted stellar mass limits, while the blue line is the best fit to the three populations combined.

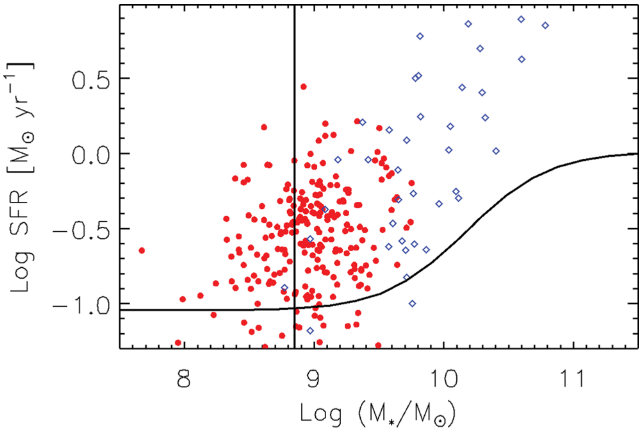

Figure 13. The SFR of all emission-line galaxies in our sample is shown as a function of their stellar mass. Our LDSS-3 data are shown as the red points; blue points are public data from FORS2 spectroscopy. The 2σ stellar mass and 5σ SFR limits are shown as solid, black lines.

which the sample should be statistically complete is determined to be $\log L_{[\mathrm{O\,II}]} \sim 39.9$. However, most of the volume is limited to higher luminosities, and $\log L_{[\mathrm{O\,II}]} \sim 40.1$ is a more representative limit for most of the data. The limiting SFR (including the mass-dependent empirical correction) can be determined from the [O II] luminosity limit, using equations (11) and (12). Fig. 13 is a plot of the empirically corrected SFRs versus stellar mass. The 2σ mass and 5σ SFR limits are indicated with solid lines. We reach SFR $\gtrsim 0.1\,\mathrm{M_\odot}$ at the low stellar masses of interest here, corresponding to a mass doubling time (assuming a recycling factor $R = 0.5$) of $t_\mathrm{d} \sim 1.3 \times 10^{10}$ yr. This is almost twice the Hubble time at $z = 0.7$, and we expect that this depth is sufficient to capture most of the star formation at these masses (e.g. Noeske et al. 2007; Gilbank et al. 2011).

4.5 Survey volume and density estimates

Our survey volume is defined by the survey area, the limiting magnitudes ($22.5 < K < 24$) and a flux limit on the emission-line detection. As in ROLES, we determine the redshift limit for which the galaxy would fall outside our K-magnitude limits, including the k-correction term

$$k_\mathrm{corr}(z) = \frac{-2.58z + 6.67z^2 - 5.73z^3 - 0.42z^4}{1 - 2.36z + 3.82z^2 - 3.53z^3 + 3.35z^4}. \tag{13}$$

The wavelength-dependent flux limit shown in Fig. 6 was similarly used to determine the redshift limits over which each detected emission line would be observable. The volume, V_max, from which a galaxy with a detected emission line could have been found was then calculated from the survey area (105.62 and 29.15 arcmin^2 for our CDFS and FIRES pointings, respectively) and the redshift space bounded by the K magnitude and noise flux limits, and the wavelength limits of our spectra. The volume, V_max, was determined for each galaxy by integrating the differential comoving volume (see Hogg 1999) between the appropriate redshift limits. The maximum ($0.62 < z < 0.885$) V_max is 4.7×10^4 Mpc^3 in the CDFS fields, and 1.3×10^4 Mpc^3 in FIRES.

The three structures are defined by the redshift limits given in Section 4.3. Interpreting the redshift limits as cosmological, removing these regions reduces the volume of our field sample by ~20 per cent. For the MS1054 cluster and CDFS walls themselves, which are decoupled from the Hubble flow, most of the galaxies are likely located within a volume that is much smaller than this cosmological volume. We will assume their line-of-sight extent is 10 Mpc (i.e. assuming a ~5 Mpc virial radius, which is still probably conservatively large). This corresponds to a volume of ~200 Mpc^{-3} for the cluster, and ~520 and ~610 Mpc^{-3} for the two CDFS walls.

4.6 ROLES and SDSS Stripe 82 data

We will compare our results with similarly selected data, from ROLES (Gilbank et al. 2010a) at $z \sim 1$, and the local Universe from our Stripe 82 analysis (Gilbank et al. 2011). Both of these samples are consistent with our present analysis in the choice of IMF, the empirical calibration of [O II] to SFR, and the removal of red, massive galaxies.[3]

The ROLES SFRs are also limited by [O II] flux, and thus the mass-dependent SFR limit has the same form as shown in Fig. 13. However, the greater luminosity distance and brighter sky at the wavelength of redshifted [O II] at $z = 1$ mean, despite the longer exposure times, that the limiting SFR at $z = 1$ is a factor of ~3 greater than in the present study. In Gilbank et al. (2011), we demonstrated that, locally, the SFRD has converged for SFR $> 0.1\,\mathrm{M_\odot\,yr^{-1}}$, for galaxies with $\log\left(M/\mathrm{M_\odot}\right) \sim 9$, and SFR $> 1\,\mathrm{M_\odot\,yr^{-1}}$ for galaxies with $\log(M) \sim 10$. Globally, the average sSFR is known to evolve approximately as $(1 + z)^{2.5}$ (e.g. Prescott, Baldry & James 2009). Assuming that the shape of the SFRD does not evolve strongly, we would expect ROLES [$\log\left(M/\mathrm{M_\odot}\right) \gtrsim 9$ at $z = 1$] to be complete at ~$0.5\,\mathrm{M_\odot\,yr^{-1}}$, and the present study [$\log\left(M/\mathrm{M_\odot}\right) \gtrsim 9$ at $z = 0.75$] to be complete at SFR $\sim 0.4\,\mathrm{M_\odot\,yr^{-1}}$. Thus, we expect that our samples are deep enough to have recovered most of the star formation in the Universe, and to be fairly insensitive to the precise choice of limiting SFR.

---

[3] In fact, the Stripe 82 analysis is based on Hα measurements of the SFR which, by construction, are consistent with the mass-dependent [O II]–SFR conversion. This avoids the incompleteness in [O II] noted by Gilbank et al. (2011) for high-mass galaxies in Stripe 82.

5 RESULTS

5.1 Star formation rate density

The SFRD was computed as follows:

$$\rho_{\mathrm{SFR}}(M_*) = \sum_{i=0}^{n} \frac{P_{\mathrm{O\,II},i} \cdot \mathrm{SFR}_i}{w_i \cdot V_{\mathrm{max},i}}, \tag{14}$$

where the SFR was calculated according to equations (11) and (12), and the sum is over all galaxies in a given bin of stellar mass. $P_{\mathrm{O\,II},i}$ is the probability that the line is [O II], relative to the probability of it being any other plausible emission line; w_i is a magnitude-dependent weight to account for incompleteness. Fig. 14 shows the SFRD for our LDSS-3 sample. Recall from Fig. 10 that our completeness drops significantly for bright ($K < 22.5$) galaxies, corresponding to $M > 3 \times 10^9\,\mathrm{M}_\odot$. Moreover, this high-mass end has no contribution from the FIRES field, and is therefore especially sensitive to cosmic variance (not included in the error bars), given the large-scale structure in the CDFS field. Finally, no aperture corrections have been applied, which means that SFRs are likely underestimated for the most massive galaxies. Thus we limit our data to $M < 3 \times 10^9\,\mathrm{M}_\odot$, and replace the higher mass measurements with the $0.6 < z < 0.8$ data of Karim et al. (2011), who used stacked radio observations in the COSMOS field to measure SFR over a wider field than we have here. They note that there is a factor of ∼2 difference in normalization between [O II]-based SFR and their analysis. To eliminate this likely systematic offset, the Karim et al. (2011) SFRD should be reduced (or our [O II] data should be increased) by this factor. However, we show the data as measured, with no rescaling applied.

We compare this with results from ROLES (Gilbank et al. 2010a) at $z \sim 1$, and the local Universe from our Stripe 82 analysis (Gilbank et al. 2011). Interestingly, the ROLES SFRD is consistent with our new data at $z \sim 0.75$, over most of the mass range, with some evidence for higher SFR at $M > 10^{10}\,\mathrm{M}_\odot$ if the SFRD from Karim et al. (2011) is reduced by a factor of ∼2 as described above. Compared with the $z \sim 0.1$ data from Stripe 82, the SFRD at both $z = 0.75$ and 1 is higher by a factor of ∼3 at all masses. Given the statistical and systematic uncertainties, though, we cannot rule out a continuous evolution of the form $\mathrm{SFRD} \propto (1+z)^{2.0}$ (e.g. Gilbank et al. 2010a), represented on Fig. 14 as the solid and dashed lines at $z = 0.75$ and 1, respectively.

Our findings are in good agreement with Karim et al. (2011) and Gilbank et al. (2010a) that there is no evidence here for strong evolution in the shape of the SFRD. We note that both ROLES and the present work hint at an increased contribution from the lowest mass galaxies for which we are complete (∼$10^9\,\mathrm{M}_\odot$), relative to the local Universe. However, any mass-dependent effect is fairly subtle, and it is unlikely that systematic uncertainties are understood to this level across the entire mass and redshift range. The data are not inconsistent with a simple, mass-independent evolution of $\mathrm{SFRD} \propto (1+z)^{2.0}$ over the redshift range $0 < z < 1$, as suggested by Gilbank et al. (2010a).

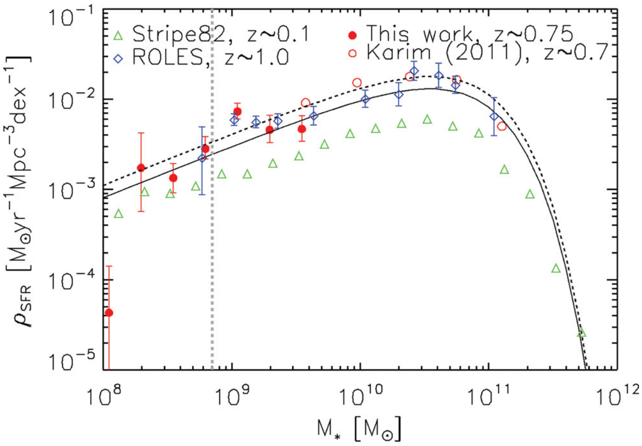

Figure 14. The SFRD of our sample, at $z \sim 0.75$, is shown as the red points with error bars at $M < 3 \times 10^9\,\mathrm{M}_\odot$. The grey vertical dashed line highlights the mass limit of the present survey. The high-mass data are taken from the stacked radio analysis of galaxies at $0.6 < z < 0.8$ from Karim et al. (2011), shown as the open circles. Note that Karim et al. (2011) find a factor of ∼2 difference in normalization between their radio-based SFRD and the [O II]-based analysis of ROLES at $z = 1$. If this is treated as a systematic effect, the solid circles of Karim et al. (2011) on this figure should be brought down by a factor of 2. This SFRD is compared with ROLES at $z = 1$ (blue diamonds), and the SDSS from our analysis of Stripe 82 data (green triangles). The solid and dashed line represent Schechter functions fit to the Stripe 82 data, scaled by a factor of $(1 + z)^2$ to $z = 0.75$ and $z = 1$.

5.2 Stellar mass function of star-forming galaxies

The GSMF for our sample of star-forming galaxies (SF-GSMF) is shown in Fig. 15. In order to study its evolution, we compare our $z \sim 0.75$ data with the Stripe 82 SDSS data as detailed in Section 4.6. The left-hand panel only considers the present $z \sim 0.75$ data above a conservative SFR limit of $0.3\,\mathrm{M}_\odot\,\mathrm{yr}^{-1}$ so as to compare directly with the depth of the slightly shallower $z \sim 1$ ROLES data. To compare fairly with the local data, the Stripe 82 sample is limited to $\mathrm{SFR} \geq 0.1\,\mathrm{M}_\odot\,\mathrm{yr}^{-1}$. Since the SFRD falls by a factor of ≈3 over this redshift interval (as discussed in Section 5.1), this cut corresponds to a similarly evolving limit. For comparison, we also show the single Schechter function fit to the SDSS star-forming population at $z = 0.1$ from Peng et al. (2010). Transforming to the Baldry & Glazebrook (2003) IMF, the parameters of this fit are $\log M_* = 10.92$ and $\Phi^* = 2.612 \times 10^{-3}\,\mathrm{dex}^{-1}\,\mathrm{Mpc}^{-3}$. The high-mass end of the SF-GSMF function ($M \gtrsim 3 \times 10^9\,\mathrm{M}_\odot$) is not very well determined in our present data, due to the limited survey area and spectroscopic sampling. At lower masses, where we expect our sample to be highly complete, the data are consistent with no evolution of the SF-GSMF from $0 < z < 1$, in agreement with the conclusions of Gilbank et al. (2010a) and Peng et al. (2010).

In the right-hand panel, the full depth of the present $z \sim 0.75$ data set is considered, down to a SFR limit of $0.1\,\mathrm{M}_\odot\,\mathrm{yr}^{-1}$. The Stripe 82 data from the left-hand panel is reproduced here, but we also show these data extended to a lower limiting $\mathrm{SFR} \geq 0.03\,\mathrm{M}_\odot\,\mathrm{yr}^{-1}$, allowing for a factor of ≈3 in SFR evolution. We also compare with data from Pozzetti et al. (2010), shown without error bars, for clarity. This sample defined star-forming galaxies as those with $\log \mathrm{sSFR/Gyr} > -1$, approximately consistent with the limits we apply to our data, here. Again we convert the result to correspond to a BG03 (Baldry & Glazebrook 2003) IMF. The results are consistent with little or no evolution in the SF-GSMF over this redshift range. However, it also demonstrates the sensitivity of any measured evolution to the limiting SFR of the samples. If we account for the global evolution of SFR we find that the SF-GSMF remains constant down to the lowest masses for which we have statistically complete samples. Choosing a fixed, non-evolving limit would result in a large decrease with increasing cosmic time of the SF-GSMF at the low-mass end. The difference between the analysis of Peng et al. (2010), where SF galaxies are identified strictly by colour, and our

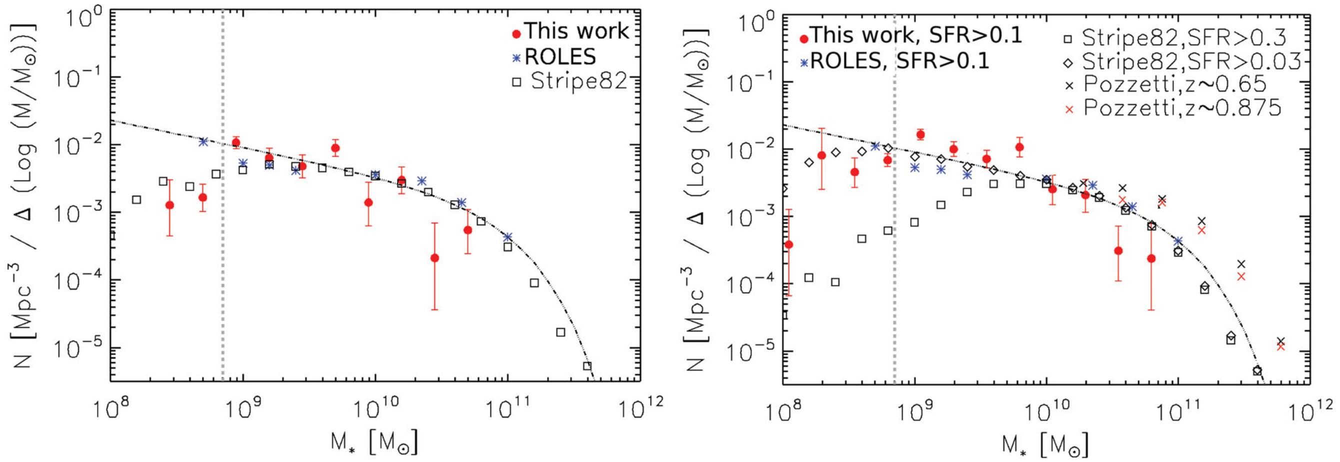

Figure 15. Left-hand panel: the stellar mass function of all star-forming galaxies with SFR $\geq 0.33\,\mathrm{M_\odot\,yr^{-1}}$ in our sample is shown as the points with error bars. This is compared with ROLES data at $z \sim 1$ (blue asterisks), to the same SFR limit, and with the SDSS Stripe 82 data to a limit of a factor of ~3 lower to account for evolution (see Gilbank et al. 2010a). The dashed line represents the Schechter function fit to the local, SDSS data by Peng et al. (2010). Right-hand panel: our data are now shown to a deeper SFR limit of SFR $\geq 0.1\,\mathrm{M_\odot\,yr^{-1}}$; this is compared to the Stripe 82 data to two different depths, as described in the legend. We also compare with data at $0.55 < z < 0.75$ and $0.75 < z < 1.0$ from Pozzetti et al. (2010), shown as black and red crosses, respectively. The thick grey vertical dashed line in both panels highlights the mass limit of the present survey.

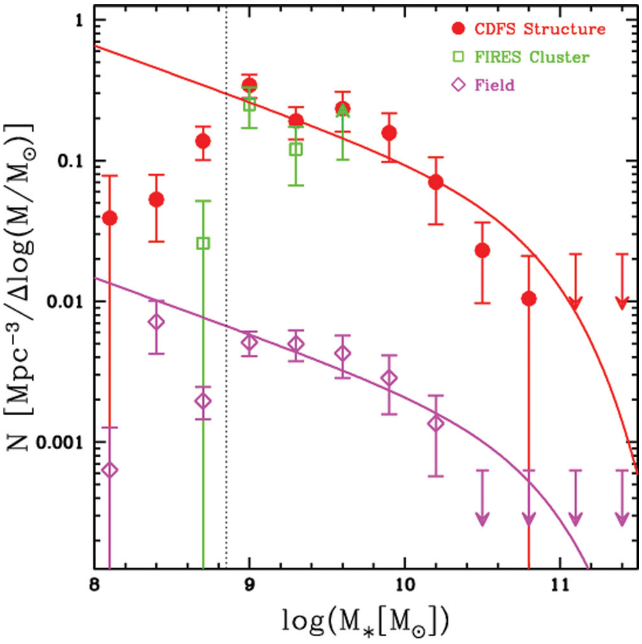

Figure 16. The stellar mass function for star-forming galaxies in our survey is shown, divided by environment as shown in the legend. Here we assume that the line-of-sight extent of both the cluster and CDFS structures is 10 Mpc (comoving). The local Schechter function for star-forming galaxies from Peng et al. (2010) has been renormalized to fit the low-density and structured environments. We see no dependence of the shape on environment. Both the cluster and CDFS 'walls' are comparable in overdensity, a factor of ~45 times denser than the field. Error bars and upper limits are 1σ. The lower limit on the most massive FIRES point is due to the lack of redshifts for $K < 22$. The vertical dotted line highlights the mass limit of the present survey.

Stripe 82 analysis, shows that remaining systematic uncertainties of this type are at least as important as any physical evolution.

In Fig. 16 we divide our sample into different environments: the MS1054 cluster in FIRES, the large-scale structure in CDFS and the remaining population which we call the 'field'. The cluster in FIRES has no public spectroscopy for $K < 22$, which means that field is incomplete for $M > 10^{9.5}\,\mathrm{M_\odot}$. Recall from Section 4.5 that the normalizations of the FIRES cluster and CDFS structures are calculated assuming a comoving line-of-sight extent of 10 Mpc. We also show the local mass function of star-forming galaxies, from Peng et al. (2010), renormalized to minimize the χ^2 value of the dense and underdense samples over the range for which the data are complete. This shows that both high-density environments are a factor of ~45 times denser than the field sample. This depends on our assumption about the line-of-sight extent. A firm lower limit to the overdensity is a factor of 7, obtained by assuming the cosmological volume between the redshift limits used to define each sample. We note that the shape of the single Schechter function, with M_* and α fixed to their local values, is a good fit to both the field and overdense samples. There is no evidence for it to vary with environment, and the reduced χ^2 is near unity for both samples.

5.3 Specific star formation rate

The sSFR of galaxies in our sample is shown as a function of their stellar mass in Fig. 17. The small filled circles represent the individual emission-line galaxies. The large symbols represent the *binned mean* sSFR of the present, combined sample (solid red circles), compared with ROLES at $z = 1$ (solid black circles), and local star-forming SDSS (blue diamonds) data sets.

We find a distinct anti-correlation between sSFR and M_*, with a power-law slope of $\beta \sim -0.2$ over the mass range of $10^9 < M_*/\mathrm{M_\odot} < 10^{10}$. This is similar to our finding at $z = 1$ with ROLES, and steeper than the anti-correlation at $z = 0$ which already poses a challenge to models (Bower, Benson & Crain 2012; Weinmann et al. 2012). At all stellar masses, the sSFR at $z = 0.75$ and 1 is significantly larger than locally. Moreover, the relation significantly departs from a simple power law, with an upturn observed at low stellar mass (see also Brinchmann et al. 2004; Elbaz et al. 2007; Popesso et al. 2011). To interpret this, we turn to the models used by Gilbank et al. (2011), based on the staged galaxy formation models of Noeske et al. (2007). These are shown as the smooth curves in Fig. 17. In this model, galaxies are parametrized by an

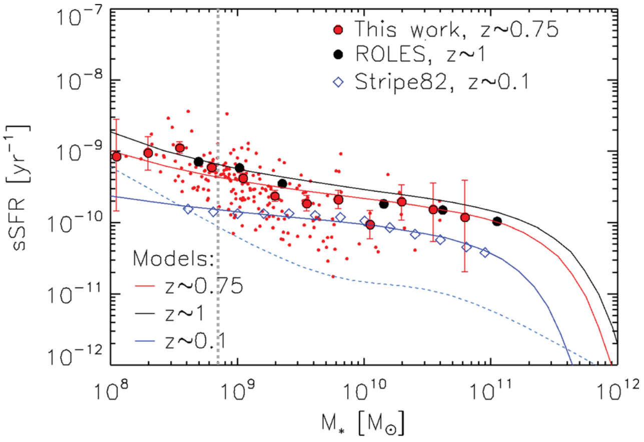

Figure 17. The sSFR of the star-forming galaxies in our sample are shown as a function of stellar mass. Small points represent individual galaxies, while the filled circles with error bars are the mean values, in equal mass bins. Comparable mean values are shown at $z = 1$ from ROLES (solid black circles), and at $0 < z < 0.1$ from Stripe 82 (Gilbank et al. 2011), without error bars for clarity. We overplot the Gilbank et al. (2011) models (see text for description) at three redshifts, as indicated in the legend. Also shown is the mass limit of this survey (thick grey vertical dashed line) and the SFR limit (dashed, light blue line).

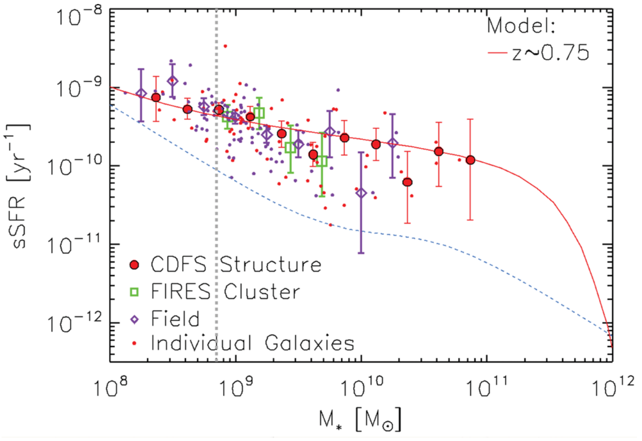

Figure 18. Same as Fig. 17, but where our data are now divided into high-density structures, the MS1054 cluster (open green squares) and field environments. We show only the Gilbank et al. (2011) model corresponding to $z = 0.75$, as the smooth, red curve.

exponentially declining SFR, with formation redshift and SFR timescales both a function of stellar mass. This simple description provides a reasonable match to the observations at all three epochs shown, including the increase in sSFR observed at the lowest stellar masses in both the present data and ROLES.

Finally, in Fig. 18 we show the sSFR–M_* relation in different environments. Both high and typical density populations show a decreasing sSFR with increasing stellar mass. The shape and normalization of the relation in all environments are consistent with one another, and with the model of Gilbank et al. (2011), over the entire stellar mass range.

6 DISCUSSION

It has consistently been shown that the main influence of environment is on the fraction of star-forming galaxies of a given stellar mass (e.g. Baldry et al. 2006; Wijesinghe et al. 2012). Amongst the star-forming population itself, any residual environment dependence is weak at best (e.g. Peng et al. 2010). However, a transformation from active to passive cannot be instantaneous and must therefore be reflected in an environmental dependence of the sSFR distribution. Results here are more controversial and depend on how the analysis was done. At low redshifts, $z \lesssim 0.5$, dense environments consistently show either no change in the sSFR relation (e.g. Peng et al. 2010) or a mildly reduced sSFR (e.g. Vulcani et al. 2010). At $z \sim 1$ and above, there is some evidence that sSFR is *higher* amongst star-forming galaxies in some dense environments, but not all (Sobral et al. 2011). While we will not resolve this issue here, our data extend the discussion to low-mass galaxies at an intermediate redshift of $z \sim 0.75$.

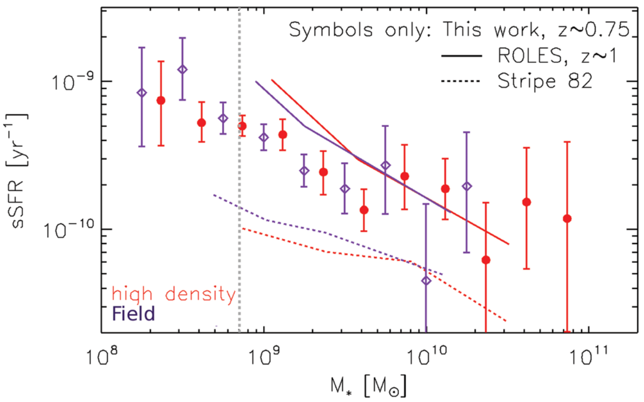

Figure 19. The mean correlation between sSFR and stellar mass is shown for our sample, as the points with error bars. The purple diamonds represent the result in the ‘field’, while the red circles represent the high-density environments (MS1054 cluster and CDFS structures), which are a factor of ~45 overdense. This is compared with similar relations at $z = 1$ (ROLES) and $z = 0$ (SDSS), taken from the analysis by Li et al. (2011). In this case, the red line only represents an overdensity of ~6 relative to the average environment, represented by the purple line. The thick grey vertical dashed line highlights the mass limit of the survey.

In Fig. 19 we re-create the density segregated, sSFR$-M_*$ plot from Li et al. (2011, their fig. 6). In this plot we show the density-dependent sSFR$-M_*$ relation for each of the $z = 0.1$ (SDSS), $z = 0.75$ (present study) and $z = 1$ (ROLES) epochs. The SDSS and ROLES samples were segregated according to a local density parameter, ρ_5, which is defined in detail[4] in Li et al. (2011). In the figure, we show only the relations for the average environment, and the most overdense subsample, for best comparison with the present data. For the ROLES sample at $z = 1$, Li et al. (2011) find that the local density ranges from 0.04 to 0.6 Mpc^{-3}, with an average of ~0.1 Mpc^{3}. Thus their overdense regions are a factor of ~6 denser than the average. We estimated the volume density of our subsamples in Section 4.3; assuming a 10 Mpc line-of-sight extent for our high-density structures, this is ~0.9 Mpc^{-3}, compared with the field value of ~0.02 Mpc^{-3}. While these numbers cannot be compared directly with ρ_5, they are not too dissimilar in practice. The small fields mean that the nearest neighbour approach taken

---

[4] Briefly, ρ_5 indicates the redshift-completeness weighted number density of star-forming galaxies limited to $M_{K_{AB}} \leq -21.0$, found within a ‘nearest neighbour’ volume defined by the five closest galaxies to the current galaxy being evaluated. The volume is defined by the maximum projected radius of the set of five nearest neighbour galaxies, and the difference in comoving distances set by the *closest* and *farthest* nearest neighbour galaxies in redshift space.

by Li et al. (2011) is almost exclusively identifying structure in redshift space, as we do here. The main difference is that Li et al. use massive galaxies as tracers, while we use low-mass emission-line galaxies. While the physical scales over which the density is estimated will not be identical, we may expect that the relative density between structures and the field can be fairly compared between the two analyses, to within a factor of a few. Thus, the high-density environments of the present study, overdense by a factor of ∼45, are likely to be significantly denser than those of Li et al. (2011). In fact, 45 is probably an underestimate, as at least the MS1054 virial diameter is likely much less than 10 Mpc.

Considering first the average, 'field' environments, Fig. 19 shows smooth evolution of the sSFR$-M_*$ relation from $z = 0$ to 1, with little or no significant change in slope, but a normalization that increases approximately as $(1 + z)^{2.5}$. In contrast, the low-mass end slope of the relation in high-density environments shows mild evolution. It is flatter than the average relation locally, and steeper than the average relation at $z = 1$. Interestingly, our new data at an intermediate redshift $z \sim 0.7$ shows no difference at all between the two environments. Since our survey includes environments with much higher densities, the actual evolution between $z \sim 0.7$ and $z \sim 1.0$ of comparably dense environments could be considerably stronger than shown here. Note that the analysis of Li et al. (2011) includes an *underdense* environment, for which the contrast with their densest environments is considerably larger.

The implication is that the sensitivity of low-mass, star-forming galaxies to their environment has evolved significantly from $z = 1$ to the present day. Today, the average sSFR of such galaxies is slightly lower in high-density environments, while at $z = 1$ the average is slightly *higher*. This 'reversal' of the SFR–environment relation has been noted by others (e.g. Elbaz et al. 2007; Li et al. 2011), and our new data at $z = 0.7$ appear to correspond to the 'transition' epoch where the sSFR–mass relation shows no environmental dependence.

7 CONCLUSIONS

For the first time, the faint [O II] emission from low stellar mass galaxies [$8.5 < \log(M_*/\mathrm{M}_{\odot}) < 9.5$] has been spectroscopically measured for galaxies in the redshift range $0.62 < z < 1.15$. By targeting fields (CDFS and FIRES) with known overdensities, including the massive MS1054−03 cluster, we explore how star formation in these low-mass galaxies is affected by their environment. Our main conclusions are as follows.

(i) There is little, if any evolution in the GSMF of [O II] luminous galaxies between $z = 0$ and $z \sim 1$.

(ii) The trend of a decreasing sSFR with increasing stellar mass has been confirmed down to unprecedented stellar masses. The normalization at $z \sim 0.75$ is similar to our earlier results at $z = 1$, and significantly higher than at $z = 0$.

(iii) The average power lase of the sSFR$-M_*$ relation is $\beta \sim -0.2$, with indication of a steeper relation at low masses. This is consistent with what we found at $z = 1$ with ROLES.

(iv) The SFRD shows little evolution between $z = 0.7$ and 1, but is consistent with the $(1 + z)^{2.0}$ evolution expected from comparison with the SDSS. The SFRD evolution is consistent with a mass-independent evolution in normalization; that is, the characteristic mass of star-forming galaxies is independent of redshift. However, we caution that systematic and statistical uncertainties preclude us from establishing the SFRD to better than a factor of ∼2 at any mass; thus there is room for relatively small, mass-dependent evolution.

(v) Environment is found not to influence the sSFR$-M_*$ relationship at any stellar mass at the epoch studied here, $z \sim 0.75$. This suggests that the SFR of star-forming galaxies is not enhanced or diminished by local density, and that the apparent reversal in correlation between environment and SFR occurs at higher redshift.

Our results on the constancy of the SF-GSMF are consistent with many previous works (e.g. Pozzetti et al. 2010; Gilbank et al. 2011), extending the results to lower masses at this intermediate redshift. In Li et al. (2011) we showed the emergence of a weak environmental dependence of the sSFR–mass relation on environment, such that the lowest mass galaxies in the densest environments show a significant excess sSFR compared to their lower density counterparts. In this work, we show the absence of this trend ≈1 Gyr later. By the present day, another 5 Gyr later, the relation has reversed, and low-mass galaxies in dense environments have lower sSFR than the average. This smooth transition is consistent with e.g. Quadri et al. (2012), who pointed out that it would be strange to see a sharp transition given factors such as the apparently smooth growth of passive galaxies over cosmic time. We note, however, that this environmental dependence of the star-forming population is very mild, and much weaker than the aforementioned evolution in the fraction of galaxies with no star formation whatsoever.

ACKNOWLEDGMENTS

We thank an anonymous referee for very helpful comments that improved the paper. The ROLES collaboration would like to thank S. Crawford, T. Dahlen, H. Dominguez, M. Franx, S. Juneau, C. Maier, B. Mobasher, L. Pozzetti, E. Vanzella and S. Wuyts for providing data and useful correspondence throughout the project. MLB acknowledges support from an NSERC Discovery Grant and an Early Researcher Award from the Province of Ontario.

REFERENCES

Baldry I. K., Glazebrook K., 2003, ApJ, 593, 258
Baldry I. K., Glazebrook K., Brinkmann J., Ivezić Z., Lupton R. H., Nichol R. C., Szalay A. S., 2004, ApJ, 600, 681
Baldry I. K. et al., 2006, MNRAS, 373, 469
Balogh M. L., Baldry I. K., Nichol R. C., Miller C., Bower R. G., Glazebrook K., 2004, ApJ, 615, L101
Bell E. F. et al., 2007, ApJ, 663, 834
Bohlin R., Lindler D., 1992, Space Telescope Sci. Inst. Newslett., 9, 19
Bolzonella M. et al., 2010, A&A, 524, A76
Bower R. G., Benson A. J., Crain R. A., 2012, MNRAS, 422, 2816
Brinchmann J., Charlot S., White S. D. M., Tremonti C., Kauffmann G., Heckman T., Brinkmann J., 2004, MNRAS, 351, 1151
Bundy K. et al., 2006, ApJ, 651, 120
Cooper M. C. et al., 2008, MNRAS, 383, 1058
Cooper M. C. et al., 2010, MNRAS, 409, 337
Cowie L. L., Songaila A., Hu E. M., Cohen J. G., 1996, AJ, 112, 839
Crawford S. M., Wirth G. D., Bershady M. A., Hon K., 2011, ApJ, 741, 98
Cucciati O. et al., 2010, A&A, 524, A2
Davies G. T. et al., 2009, MNRAS, 395, L76
Elbaz D. et al., 2007, A&A, 468, 33
Fioc M., Rocca-Volmerange B., 1997, A&A, 326, 950
Förster Schreiber N. M. et al., 2006, AJ, 131, 1891
George M. R. et al., 2011, ApJ, 742, 125
Gerke B. et al., 2007, MNRAS, 376, 1425
Gilbank D. G. et al., 2010a, MNRAS, 405, 2419
Gilbank D. G., Baldry I. K., Balogh M. L., Glazebrook K., Bower R. G., 2010b, MNRAS, 405, 2594
Gilbank D. G. et al., 2011, MNRAS, 414, 304
Gilli R. et al., 2003, ApJ, 592, 721

Glazebrook K., Bland-Hawthorn J., 2001, PASP, 113, 197
Glazebrook K. et al., 2004, Nat, 430, 181
Grützbauch R., Conselice C. J., Varela J., Bundy K., Cooper M. C., Skibba R., Willmer C. N. A., 2011, MNRAS, 411, 929
Hogg D., 1999, preprint (astro-ph/9905116)
Ideue Y. et al., 2009, ApJ, 700, 971
Karim A. et al., 2011, ApJ, 730, 61
Kennicutt R. C., 1998, ARA&A, 36, 189
Le Fèvre O. et al., 2004, A&A, 428, 1043
Li I. H. et al., 2011, MNRAS, 411, 1869
McGee S. L., Balogh M. L., Wilman D. J., Bower R. G., Mulchaey J. S., Parker L. C., Oemler A., 2011, MNRAS, 413, 996
Mobasher B. et al., 2009, ApJ, 690, 1074
Muldrew S. I. et al., 2012, MNRAS, 419, 2670
Muzzin A. et al., 2012, ApJ, 746, 188
Noeske K. G. et al., 2007, ApJ, 660, L47
Patel S. G., Kelson D. D., Holden B. P., Franx M., Illingworth G. D., 2011, ApJ, 735, 53
Peng Y. et al., 2010, ApJ, 721, 193
Popesso P. et al., 2011, A&A, 532, 145
Pozzetti L. et al., 2010, A&A, 523, A13
Prescott M., Baldry I. K., James P. A., 2009, MNRAS, 397, 90
Quadri R. F., Williams R. J., Franx M., Hildebrandt H., 2012, ApJ, 744, 88
Ravikumar C. D. et al., 2007, A&A, 465, 1099
Salpeter E. E., 1955, ApJ, 121, 161
Sobral D., Best P., Smail I., Geach J., Cirasuolo M., Garn T., Dalton G. B., 2011, MNRAS, 411, 675
Strateva I., Ivezić Ž. et al., 2001, AJ, 122, 1861
van Dokkum P. G., Franx M., Fabricant D., Illingworth G. D., Kelson D. D., 2000, ApJ, 541, 95
Vanzella E. et al., 2005, A&A, 434, 53
Vanzella E. et al., 2008, A&A, 478, 83
Vulcani B., Poggianti B. M., Finn R. A., Rudnick G., Desai V., Bamford S., 2010, ApJ, 710, L1
Weinmann S. M., Pasquali A., Oppenheimer B. D., Finlator K., Mendel J. T., Crain R. A., Maccio A. V., 2012, preprint (arXiv:1204.4184)
Wijesinghe D. B. et al., 2012, MNRAS, 423, 3679
Wolf C. et al., 2009, MNRAS, 393, 1302
Wuyts S., Labbé I., Förster Schreiber N. M., Franx M., Rudnick G., Brammer G. B., van Dokkum P. G., 2008, ApJ, 682, 985

This paper has been typeset from a TEX/LATEX file prepared by the author.